Chemical Science

ROYAL SOCIETY OF CHEMISTRY

EDGE ARTICLE

View Article Online
View Journal | View Issue

Cite this: *Chem. Sci.*, 2025, **16**, 15075

All publication charges for this article have been paid for by the Royal Society of Chemistry

Promoting cationic redox and stabilizing lattice oxygen in an Fe-based DRX cathode by the synergy of initial Li deficiency and 3D hierarchical porous architecture†

Wenjie Ma,[a] Yakun Tang,*[a] Yue Zhang,[a] Xiaohui Li,[a] Lang Liu,*[a] Xueting Wang[a] and Yuliang Cao[ab]

Anionic and cationic redox chemistries boost the ultrahigh specific capacity of Fe-based disordered rock salt (DRX) Li_2FeTiO_4. However, the sluggish kinetics and high O redox activity result in continuous capacity decay and poor rate performance. Herein, 3D hierarchical porous Li_2FeTiO_4 (H-Ca-LFT) with initial Li-deficiency is successfully prepared using an acid-assisted $CaCO_3$ template method. By introducing Li deficiency, the local electronic structure of Li_2FeTiO_4 is modulated to facilitate Li^+ diffusion and regulate the redox activity. Specifically, Li deficiency reduces the density of states in the O 2p band, Li^+ diffusion barrier, and band gap, thereby suppressing the high activity of oxygen and improving transport dynamics and electron conductivity. Moreover, the 3D hierarchical porous structure provides abundant channels and active sites for ion diffusion and electrochemical reaction. The synergistic effect of Li deficiency and the 3D hierarchical porous structure is revealed by various *in/ex situ* characterizations and DFT calculations, which promotes cationic redox and stabilizes anionic redox. Consequently, H-Ca-LFT demonstrates a high initial capacity (209.3 mA h g^{-1} at 50 mA g^{-1}), remarkable rate capability (130.4 mA h g^{-1} at 1 A g^{-1}), and outstanding long-term cycling stability. This work offers a new insight into stabilizing anionic redox through the design of initial Li deficiency and 3D hierarchical porous architecture for high-performance DRX cathodes.

Received 8th May 2025
Accepted 9th July 2025

DOI: 10.1039/d5sc03335g

rsc.li/chemical-science

Introduction

With the rapid development of electric vehicles and mobile electronic devices, the energy density and capacity of lithium-ion batteries (LIBs) need to be further improved.[1,2] In recent years, the disordered rock-salt (DRX) cathodes in coordination with cation–anion redox reactions have shown high capacities (>250 mA h g^{-1}) and energy densities (>900 W h kg^{-1}), demonstrating their significant application prospects.[3,4] The unique structure of DRX breaks the elemental constraints and can accommodate various transition metals (TM) and anions within the lattice, which greatly enriches the space for material composition adjustment and brings substantial benefits for low-cost material design.[5–7] Moreover, DRX materials show significant advantages over traditional layered materials because of their relatively small interlayer repulsion force during the extraction of large quantities of Li^+, thus minimizing the interlayer structural changes and maintaining structural stability.[8,9]

Delightedly, the design and synthesis of DRX materials have made notable progress. Cathodes with iron (Fe) as the cation redox active center and titanium (Ti) as an effective high-valence charge compensator have been identified as the most promising options based on cost-effectiveness and resource sustainability considerations.[10,11] Nevertheless, the diffusion of Li^+ in these materials is slow because of the random cation distribution that restricts the diffusion paths.[12] Besides, the high redox potential of $Fe^{3+/4+}$ leads to substantial band overlap between Fe 3d and O 2p orbitals, causing overcompensation of oxygen redox capacities and irreversible oxygen loss.[13] Ultimately, the slow kinetics and elevated redox activity result in unsatisfactory capacity, significant voltage hysteresis, and poor rate capability and cycling ability.[14,15] Therefore, improving kinetics, minimizing reliance on oxygen, and promoting cationic redox contributions are crucial for developing high-performance DRX materials.

At present, the main strategies to solve the above problems are anion substitution (F,[16] Cl[17]) and surface coating (Al_2O_3,[18]

[a]*State Key Laboratory of Chemistry and Utilization of Carbon Based Energy Resources, Key Laboratory of Energy Materials Chemistry, Ministry of Education, College of Chemistry, Xinjiang University, Urumqi 830017, Xinjiang, China. E-mail: yktang@xju.edu.cn; liulang@xju.edu.cn*

[b]*College of Chemistry and Molecular Sciences, Hubei Key Laboratory of Electrochemical Power Sources, Wuhan University, Wuhan 430072, Hubei, China*

† Electronic supplementary information (ESI) available. See DOI: https://doi.org/10.1039/d5sc03335g

$LiNbO_3$,[19] LiF[20]). Specifically, anion substitution can induce Li^+ aggregation, reduce the valence state of the redox TM and stabilize TM–O bonds and the anionic framework, thereby improving the percolation efficiency and enhancing the redox capacity of the cation.[21,22] On the other hand, surface coating has shown its ability to stabilize the surface structures and avoid side reactions through the shielding effect, thereby increasing the comprehensive electrochemical performance and alleviating capacity degradation.[23] However, the presence of the local Li-rich structure hampers the complete utilization of Li, and an increased doping concentration can lead to phase separation, which negatively impacts electrochemical activity and structural stability.[24] Besides, controlling the thickness and uniformity of the coating layer presents challenges. If the coating layer does not bond tightly with the substrate, it may detach during cycling, resulting in a loss of function.[25] Therefore, to suppress irreversible oxygen redox and promote the diffusion of Li^+, it is crucial to develop more modification methods to adjust the intrinsic structural characteristics of materials. Li-deficient engineering offers a promising approach by reducing the Li–O–Li configurations, thereby achieving reversible anionic redox and fostering a stable electrode/electrolyte interface.[26] Besides, the introduction of Li deficiency can reduce the diffusion barrier for Li^+, improving the utilization of Li and optimizing the role of cationic redox.[27] Therefore, Li-deficient engineering is an effective strategy to modulate cation–anion redox performance and improve kinetics.

On the basis of this intrinsic modification strategy, the acid-assisted $CaCO_3$ template method is used to fabricate Fe-based DRX (H-Ca-LFT), characterized by an initial Li-deficient and 3D hierarchical porous structure, which serves as an effective cathode for LIBs. This cathode presents superb electrochemical performance, featuring a large storage capacity, outstanding rate performance, and excellent cycling stability. Structure analysis proved that the Li deficiency can not only promote efficient ion diffusion and enhance electronic conductivity but also suppress the high activity of oxygen. In addition, the 3D hierarchical porous structure also provides additional active sites for Li^+ storage and improves the contact area between electrolytes and electrode materials. The obtained H-Ca-LFT cathode delivers a high initial specific capacity of 209.3 mA h g^{-1} with an energy density of 470.5 W h kg^{-1} and it retains a capacity of 178.7 mA h g^{-1} (85.4% retention) and energy density of 466.5 W h kg^{-1} (99.1% retention) at 50 mA g^{-1} after 100 cycles. Even at a high current density of 1.0 A g^{-1}, the capacity retention of H-Ca-LFT remains at 72.7% (91.7 mA h g^{-1}), highlighting the impressive long-term cycle stability. This structural design offers a fresh way forward in high-performance DRX materials for energy storage.

Results and discussion

The preparation process for H-Ca-LFT is illustrated in Fig. 1a. The Li_2FeTiO_4 (LFT1) precursor was synthesized *via* the sol–gel method, employing a 1 : 1 molar ratio of citric acid to Fe^{3+}, as described in our previous publication.[28] Briefly, the dispersion containing LFT1 precursor and nano-$CaCO_3$ is quickly frozen into a solid in a freeze dryer, annealed, and acid-washed with a HCl solution to obtain H-Ca-LFT. In order to illustrate the effect of the nano-$CaCO_3$ template and the HCl solution pickling, control samples Ca-LFT and H-LFT were prepared, respectively. Further details are described in the experimental section (ESI†). According to the XRD patterns in Fig. 1b, all samples match the typical rock-salt structure of Li_2FeTiO_4, indexed to the $Fm\bar{3}m$ space group (PDF#97-018-3562). Notably, compared with Ca-LFT, the intensity of the diffraction peaks for H-LFT and H-Ca-LFT is reduced, showing that structural deficiency has been produced after acid etching, but the host structure is not destroyed.[12]

The ratios of metal elements for Ca-LFT, H-LFT, and H-Ca-LFT were determined using an inductively coupled plasma optical emission spectrometer (ICP-OES), as shown in Table S1.† The Li content in H-LFT and H-Ca-LFT is lower than that in Ca-LFT, suggesting that H^+/Li^+ exchange occurred during the HCl solution pickling process, resulting in partial replacement of Li^+ by H^+ on the surface and the formation of Li deficiency.[29] In addition, the changes in surface composition were detected by X-ray photoelectron spectroscopy (XPS). The spectral data reveal the presence of Li, Fe, Ti, O, and C elements in all samples, with the characteristic peaks at 55.2, 710.9, 457.3, 531.1 and 284.8 eV (Fig. S1†). The intensity of the Li 1s spectra for H-LFT and H-Ca-LFT is weaker than that of Ca-LFT, which is attributed to the partial Li^+ loss from the surface due to the H^+/Li^+ exchange, resulting in an abundance of Li deficiency (Fig. 1c).[30] In Fig. 1d, the O 1s spectra for all samples show three peaks located at 529.8 (lattice O^{2-}), 531.7 and 533.6 eV (adsorbed oxygen species).[31] Notably, the peak of lattice O^{2-} for H-LFT and H-Ca-LFT shifts 0.4 eV towards a more positive binding energy, likely due to insufficient coordination capacity of oxygen as a result of substantial lithium loss.[32]

As shown in Fig. 1e, the Fe 2p spectra for H-LFT and H-Ca-LFT shift toward higher binding energy compared with Ca-LFT, in which the two peaks at about 711.2 and 713.6 eV are attributed to Fe^{2+} $2p_{3/2}$ and Fe^{3+} $2p_{3/2}$, respectively.[8] The ratios of Fe^{2+}/Fe^{3+} for Ca-LFT, H-LFT, and H-Ca-LFT are 2.11, 1.52, and 1.43, respectively, demonstrating that the presence of Li deficiency increases the average valence of Fe. In addition, the C 1s spectrum for H-Ca-LFT is decomposed into four types of carbon peaks, which correspond to C–C (284.8 eV), C–O (286.5 eV), C=O (288.3 eV), and O–C=O (290.1 eV) bonds, respectively (Fig. 1f).[33] The peak intensity of O–C=O for H-Ca-LFT is lower than that for Ca-LFT, suggesting that the HCl solution treatment significantly decreased the content of carbonate. The Ti 2p spectra for all samples display two main peaks located at 458.6 and 464.4 eV, which are assigned to Ti^{4+} $2p_{3/2}$ and Ti^{4+} $2p_{1/2}$, respectively (Fig. 1g).[34] The above analysis results show that a proton exchange reaction occurs in the process of HCl solution treatment, resulting in the introduction of Li deficiency. In order to maintain the overall charge balance of materials, Fe is oxidized, resulting in an increased overall valence state.

As shown in Fig. 1h, the nitrogen isothermal adsorption curves of the samples present an obvious hysteretic loop, which is a typical feature of mesoporous materials. The specific

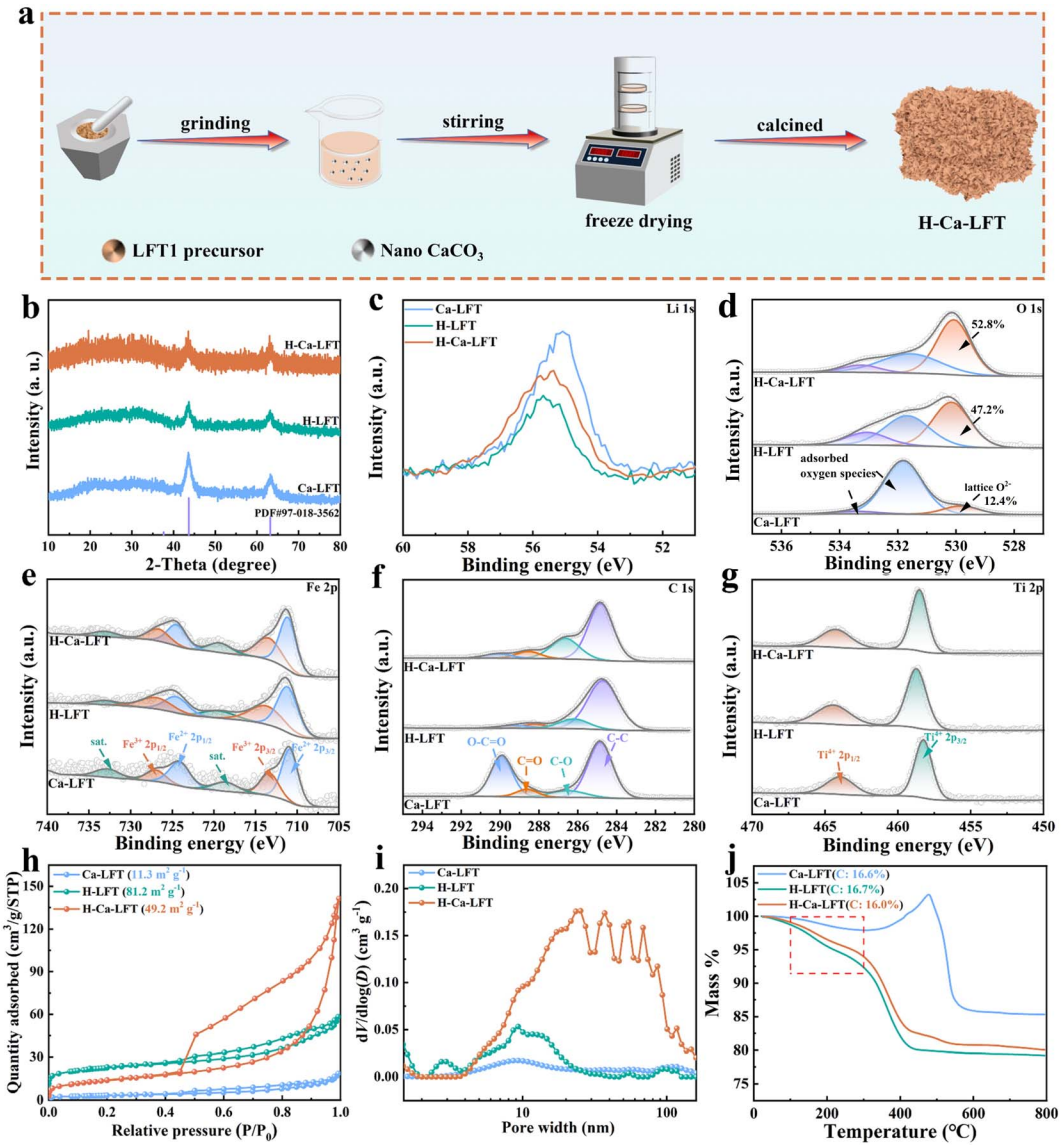

Fig. 1 (a) Schematic diagram of the formation process of H-Ca-LFT, (b) XRD, (c) Li 1s, (d) O 1s, (e) Fe 2p, (f) C 1s, (g) Ti 2p, (h) N_2 adsorption–desorption isotherms, (i) pore size distribution and (j) TG curves of Ca-LFT, H-LFT, and H-Ca-LFT.

surface areas of Ca-LFT, H-LFT and H-Ca-LFT are 11.3, 81.2 and 49.2 $m^2\ g^{-1}$, respectively. After acid etching, a large number of microporous structures are formed, which contribute to a high specific surface area. Meanwhile, the CO_2 produced by the decomposition of $CaCO_3$ leads to a sudden increase in the internal pressure of H-Ca-LFT, resulting in an enlargement of pore size and the formation of more abundant mesopores and macropores (Fig. 1i). Therefore, the specific surface area of H-Ca-LFT is lower than that of H-LFT. Among them, micropores contribute significantly to a larger specific surface area, which can provide abundant active sites for electrochemical reactions; mesopores provide rapid diffusion channels for ions, and macropores help to accommodate more active substances. The synergy of the multistage pore structure facilitates electrolyte penetration and ion diffusion, thereby improving the electrochemical performance of the electrode material.

As shown in Fig. 1j, H-LFT and H-Ca-LFT exhibit obvious weight loss in the range of 100–300 °C, which corresponds to the loss of H^+ from the crystal lattice, indicating that the proton exchange process occurs during treatment with the HCl solution.[35] Furthermore, the mass of Ca-LFT increases significantly above 400 °C, while the changes in mass for H-LFT and H-Ca-LFT are minimal. This distinct behavior stems from the differences in the pore structure of the materials. In an oxygen atmosphere, Li_2FeTiO_4 is oxidized to generate $LiFeTiO_4$ and Li_2O, resulting in a weight gain of 4.4%. H-LFT and H-Ca-LFT etched by the HCl solution form a well-developed pore structure, which significantly accelerates the diffusion of oxygen and the oxidation of carbon, enabling them to basically complete the oxidation process at around 400 °C. However, the underdeveloped pore structure of Ca-LFT is not conducive to the transportation of oxygen, resulting in a slow oxidation of

carbon. As a result, the mass of Ca-LFT increases significantly above 400 °C and reaches a weightlessness equilibrium at about 600 °C. Based on the TG curves, the carbon contents of Ca-LFT, H-LFT and H-Ca-LFT are 16.6%, 16.7% and 16.0%, respectively.

The detailed morphology of the three samples was revealed using a scanning electron microscope (SEM). As shown in Fig. 2a–c, all samples consisted of tiny nanoparticles. After acid etching, the surface of H-LFT shows abundant pore structures, while H-Ca-LFT displays a honeycomb-like structure with interconnected pores, where the mesopores and macropores are distributed throughout the specimen. TEM images also show similar structural features (Fig. 2d–f). Compared with Ca-LFT and H-LFT, H-Ca-LFT has a relatively transparent texture, and porous structures are spread throughout the whole block, forming a 3D porous network. The favorable 3D hierarchical porous structure of H-Ca-LFT mainly originates from acid etching and decomposition of nano-$CaCO_3$, which significantly increases the porosity of the material. The high-resolution images correspond to the (200) plane of Li_2FeTiO_4 (Fig. 2g–i). In addition, the discontinuous lattice fringes further confirm that H-LFT (Fig. 2h) and H-Ca-LFT (Fig. 2i) have crystal defects, providing additional diffusion paths for ions.[36,37] Accordingly, the selected area electron diffraction (SAED) pattern shows three diffraction rings corresponding to the (111), (200), and (220) planes in Ca-LFT, suggesting good crystallinity (inset in Fig. 2g). However, H-LFT and H-Ca-LFT show two weak and widened diffraction rings, indicating the existence of lattice deficiency (insets in Fig. 2h and i). Furthermore, the energy dispersive spectroscopy (EDS) elemental mappings demonstrate the homogeneous distribution of Fe, Ti, O, and C within all samples (Fig. S2† and 2j).

The electrochemical performances of the as-synthesized cathode materials were evaluated using coin-type cells with a voltage range of 1.5 to 4.8 V. As shown in Fig. 3a, the initial

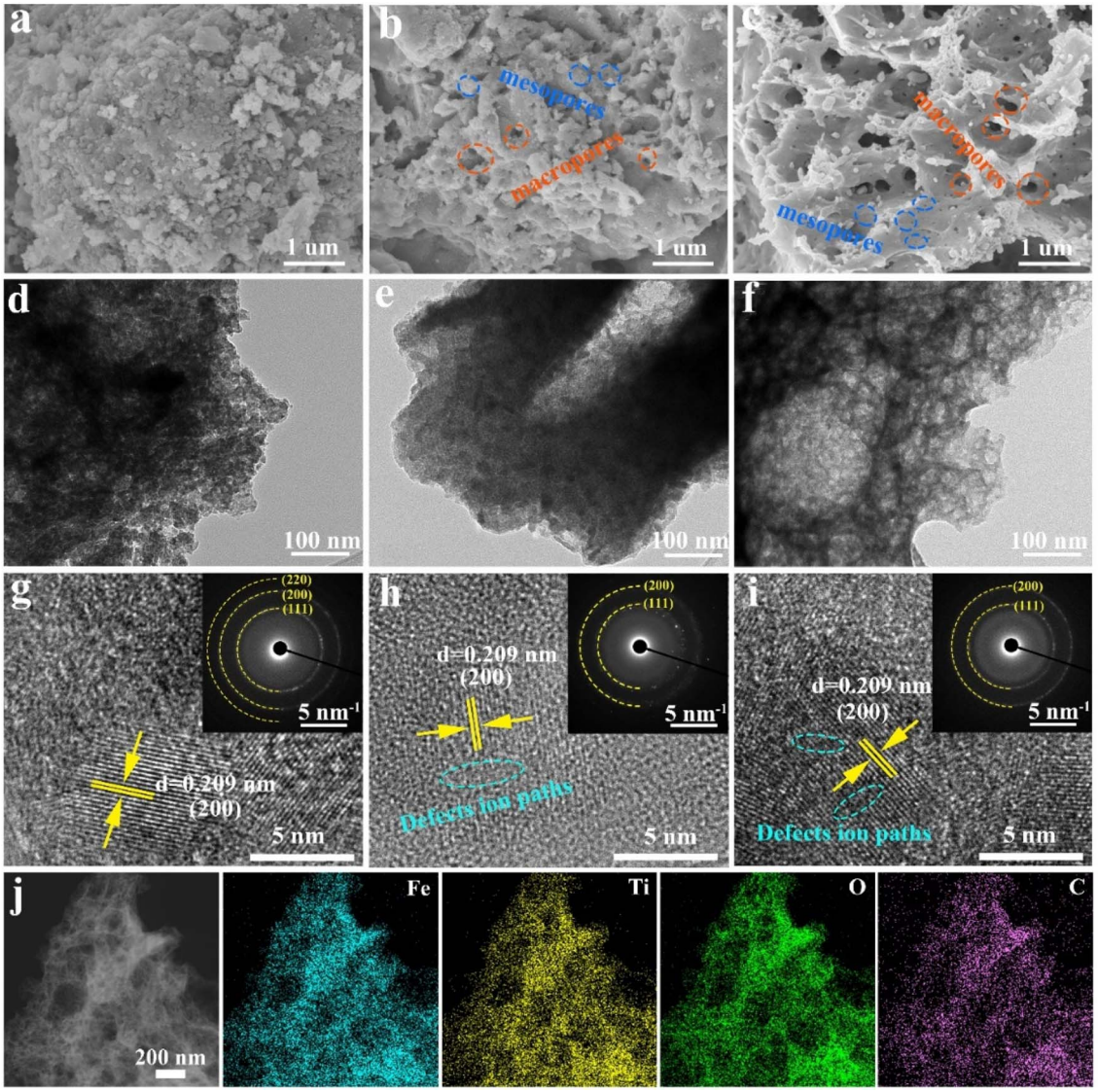

Fig. 2 SEM, TEM, and HRTEM images and SAED patterns (inset) of (a, d and g) Ca-LFT, (b, e and h) H-LFT, and (c, f and i) H-Ca-LFT, and (j) EDS mapping images of H-Ca-LFT.

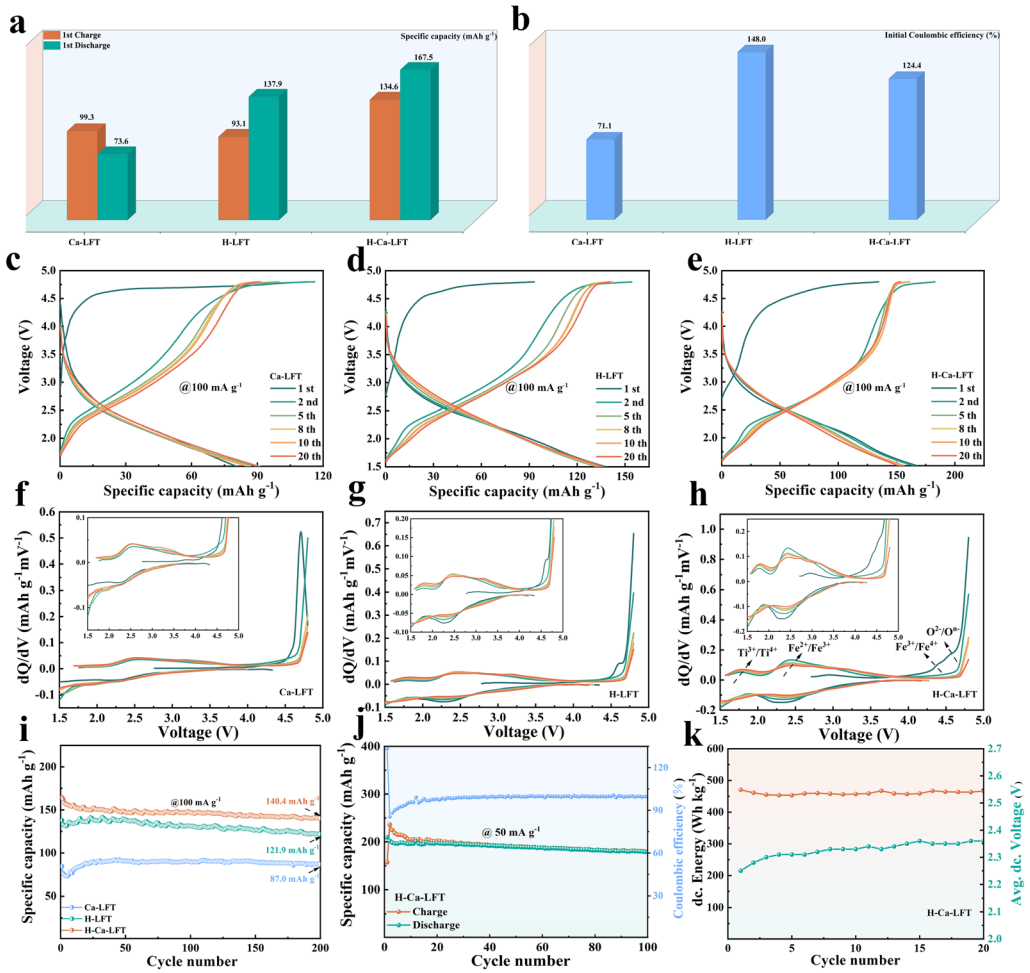

Fig. 3 (a) Initial charge–discharge specific capacities, (b) corresponding ICE, (c–e) the galvanostatic charge–discharge profiles, (f–h) corresponding dQ/dV curves, (i) cycling performances at 100 mA g^{-1} of Ca-LFT, H-LFT, and H-Ca-LFT, (j) cycling performance at 50 mA g^{-1}, and (k) discharge specific energy and average discharge voltage of H-Ca-LFT.

charge/discharge capacities of H-Ca-LFT are 134.6/167.5 mA h g^{-1}, which are significantly higher than those of Ca-LFT (99.3/73.6 mA h g^{-1}) and H-LFT (93.1/137.6 mA h g^{-1}). The excellent performance of H-Ca-LFT can be attributed to its 3D hierarchical porous structure, which optimizes ion transport, enhances electrolyte wettability, and promotes electrochemical reactions. Due to the existence of Li deficiency in the structures of H-LFT and H-Ca-LFT, the Li metal anode replenishes the Li-deficient cathode at the end of the first cycle, resulting in their initial coulombic efficiencies (ICE) exceeding 100% (Fig. 3b).[38] However, due to the unsuppressed activity of lattice oxygen and poor kinetics, the ICE of Ca-LFT is only 71.1%.[39] The galvanostatic charge–discharge profiles of Ca-LFT, H-LFT, and H-Ca-LFT at 100 mA g^{-1} during the first twenty cycles are shown in Fig. 3c–e. The initial voltage profiles of all samples exhibit typical characteristics of Fe-based DRX cathodes, featuring sloping regions (~4.4 V) associated with Fe oxidation, followed by a long plateau region (≥4.5 V) associated with O oxidation. However, due to the reduction of Li–O–Li configuration and the high stability of O–H bonds, the platform length for H-LFT and H-Ca-LFT is shorter than that for Ca-LFT.

Additionally, the voltage is decomposed into four regions (1.5–2.1, 2.1–3.5, 3.5–4.5, and 4.5–4.8 V) by different color bars to further analyze the charging capacity contribution. Obviously, the first-cycle charge capacity of all samples primarily occurs above 4.5 V, which is related to the anionic oxidation reaction (Fig. S3a–f†). In the voltage range of 4.5–4.8 V, H-Ca-LFT accounts for 60.0% (80.8 mA h g^{-1}) of the total capacity, which is significantly lower than those of Ca-LFT (88.7%, 100.0 mA h g^{-1}) and H-LFT (76.3%, 71.1 mA h g^{-1}), indicating that Li deficiency combined with 3D hierarchical porous structure may help alleviate irreversible oxygen loss. From the second cycle, the oxidation reaction degree of Fe ($Fe^{2+} \rightarrow Fe^{3+}$) and Ti ($Ti^{3+} \rightarrow Ti^{4+}$) in H-Ca-LFT gradually increased, indicating that the redox activity of TM cations becomes gradually activated and remains relatively stable after five cycles. Delightfully, H-Ca-LFT obtains a high capacity of 153.3 mA h g^{-1} after 20 cycles, and its capacity contribution in the 4.5–4.8 V range decreases to 6.2%, indicating that the main factor contributing to the rise in charge capacity is related to the cationic oxidation occurring below 4.5 V.

Similarly, the discharge voltage profiles are divided into three regions (4.8–3.0, 3.0–2.0, and 2.0–1.5 V) as shown in Fig. S4a–f.† The discharge capacity of all samples remained stable starting from the second cycle. Moreover, the discharge capacity mainly comes from the reduction reaction of TM ions below 3.0 V ($Fe^{3+} \rightarrow Fe^{2+}$ and $Ti^{4+} \rightarrow Ti^{3+}$). In the 20th discharge cycle, H-Ca-LFT shows a higher capacity (153.5 mA h g^{-1}) than those of Ca-LFT (90.5 mA h g^{-1}) and H-LFT (136.3 mA h g^{-1}). This represents contributions of 12.5% (19 mA h g^{-1}), 51.5% (78.1 mA h g^{-1}), and 36.0% (54.6 mA h g^{-1}) of the total capacity over the ranges of 4.8–3.0, 3.0–2.0, and 2.0–1.5 V, respectively. Therefore, the Li deficiency and 3D hierarchical porous structure provide efficient diffusion pathways for the electrolyte and ions, promoting efficient electrochemical reactions and increasing the capacity.

To elucidate the electrochemical lithium storage process of Ca-LFT, H-LFT, and H-Ca-LFT, the dQ/dV curves for the first twenty cycles are shown in Fig. 3f–h. Take H-Ca-LFT as a sample, for which a broad oxidation peak appears in the voltage range of 4.0–4.6 V, corresponding to the redox reactions of Fe^{3+}/Fe^{4+} and O^{2-}/O^{n-}.[40] Due to the overlap between the energy bands of $Fe^{3+/4+}$ and O^{2-}, the oxidation peak presents a broad peak.[41] In the subsequent cycle, the reversibility and intensity of the oxidation peaks of $Ti^{3+/4+}$ (1.8 V) and $Fe^{2+/3+}$ (2.4 V) are superior to those of Fe^{3+}/Fe^{4+} and O^{2-}/O^{n-}, indicating that the redox of transition metal cations is dominant at low voltage. It is worth noting that the voltage difference (ΔV) between the anodic and cathodic peaks can reflect the reversibility and polarization degree of electrode materials during the charge/discharge process. The Li-deficient engineering modulates the local electronic structure, achieving rapid Li^+ diffusion and charge transfer and reducing electrochemical polarization. As a result, the ΔV for H-Ca-LFT is 0.06 V after 20 cycles, which is narrower than that of Ca-LFT (0.18 V) and H-LFT (0.12 V), indicating that Li deficiency in conjunction with 3D hierarchical porous structure promote rapid diffusion and charge transfer of Li^+, thereby reducing electrochemical polarization. In addition, the cyclic voltammetry curves also confirm the highly reversible redox reaction of H-Ca-LFT (Fig. S5c†), showing the strongest redox peaks compared to Ca-LFT (Fig. S5a†) and H-LFT (Fig. S5b†).

As shown in Fig. 3i, the cycling performances for all samples are evaluated at 100 mA g^{-1} in the voltage range of 1.5–4.8 V. H-Ca-LFT delivers a higher specific capacity of 140.4 mA h g^{-1} than those of Ca-LFT (87.0 mA h g^{-1}) and H-LFT (121.9 mA h g^{-1}) after 200 cycles. The excellent performance of H-Ca-LFT is mainly attributed to the enhanced dynamics of ion and electron transport and improved Li utilization due to Li deficiency. Furthermore, its 3D hierarchical porous structure provides abundant diffusion channels. Remarkably, H-Ca-LFT exhibits a high initial discharge capacity of 209.3 mA h g^{-1} with a capacity retention of 85.4% (178.7 mA h g^{-1}) at 50 mA g^{-1} after 100 cycles, accompanied by a coulombic efficiency (CE) of 99.8% (Fig. 3j), competing with other reported DRX cathodes (Tables S3 and S4†). Furthermore, the discharge energy density for H-Ca-LFT decreases from 470.5 to 466.5 W h kg^{-1} with a high energy retention of 99.1%, while the average discharge voltage increases by 0.11 V from 2.25 to 2.36 V after 20 cycles (Fig. 3k). The Li deficiency and 3D hierarchical porous structure can promote the diffusion kinetics of Li^+ at high current density, improving the electrochemical activity. H-Ca-LFT shows superior rate performance compared to Ca-LFT and H-LFT, as evidenced by its maximum restored capacity at various current densities. Especially, H-Ca-LFT delivers an average discharge capacity of 130.4 mA h g^{-1} at 1 A g^{-1}, much higher than those of Ca-LFT (55.2 mA h g^{-1}) and H-LFT (96.2 mA h g^{-1}). Meanwhile, the specific capacity of H-Ca-LFT can be restored to 164.0 mA h g^{-1} even when the rate recovers to 0.1 A g^{-1}, demonstrating its favorable electrochemical reaction kinetics (Fig. 4a).

Furthermore, to reveal the evolution of the Li^+ transport kinetics in Ca-LFT, H-LFT, and H-Ca-LFT, *in situ* electrochemical impedance spectra (*in situ* EIS) were employed during the first cycle. The EIS spectra of all samples are shown in Fig. S6a–f.† The high-to-medium frequency region corresponds to the diffusion of Li^+ in the interfacial layer (R_f) and the charge transfer resistance (R_{ct}), while the sloping line is related to the Warburg resistance (R_w). Obviously, R_{ct} of H-Ca-LFT in the range of open circuit voltage (OCV) to 4.6 V is smaller than those of Ca-LFT and H-LFT, indicating a faster charge transfer process (Fig. 4b). Since proton exchange mainly occurs in the surface region of the materials, an increased concentration of H^+ in the surface lattice hinders the migration of Li^+ at high voltage.[42] R_{ct} of H-Ca-LFT increases dramatically when charging to 4.8 V. However, H-Ca-LFT exhibits a smaller R_f (46.8 Ω) than those of Ca-LFT (151.9 Ω) and H-LFT (59.7 Ω), indicating its enhanced interface Li^+ transport and charge transfer process (Fig. 4c). The high R_f of Ca-LFT is attributed to the highly active oxygen that triggers a severe interfacial side reaction, forming a non-conductive solid electrolyte interphase that blocks the Li-migration channels.[43,44] Because the diffusion process within the electrodes gradually becomes limited with the insertion of Li^+, R_{ct} for all electrodes gradually increases during the discharging process. Notably, R_{ct} of H-Ca-LFT is lower and more stable than that of Ca-LFT and H-LFT, revealing that the Li-deficient and high porosity of H-Ca-LFT improve the Li^+ transport kinetics.

The Li^+ diffusion coefficient (D_{Li^+}) for all samples in the first cycle is evaluated by the galvanostatic intermittent titration technique (GITT). As shown in Fig. 4d, the average D_{Li^+} of H-Ca-LFT is 1.37×10^{-12} cm^2 s^{-1}, which is higher than those of the Ca-LFT (1.30×10^{-14} cm^2 s^{-1}) and H-LFT (5.87×10^{-14} cm^2 s^{-1}). It is noteworthy that H-Ca-LFT exhibits higher values than Ca-LFT and H-LFT at about 4.3 V and 4.6 V, indicating fast kinetics of the Fe^{3+}/Fe^{4+} and O^{2-}/O^{n-} redox reactions. Similarly, H-Ca-LFT also exhibits rapid Li^+ diffusion during discharge, with an average D_{Li^+} of 2.88×10^{-12} cm^2 s^{-1}, which is much higher than those of Ca-LFT (6.17×10^{-14} cm^2 s^{-1}) and H-LFT (1.05×10^{-12} cm^2 s^{-1}) (Fig. 4e). The abundance of pore structure and active sites endows H-Ca-LFT with a faster ion diffusion rate, which is consistent with the analysis result of *in situ* EIS. H-Ca-LFT delivers a high capacity of 125.4 mA h g^{-1} with a capacity retention of 74.5% at 500 mA g^{-1} after 600 cycles. As shown in Fig. S8,† the morphology of the H-Ca-LFT electrode

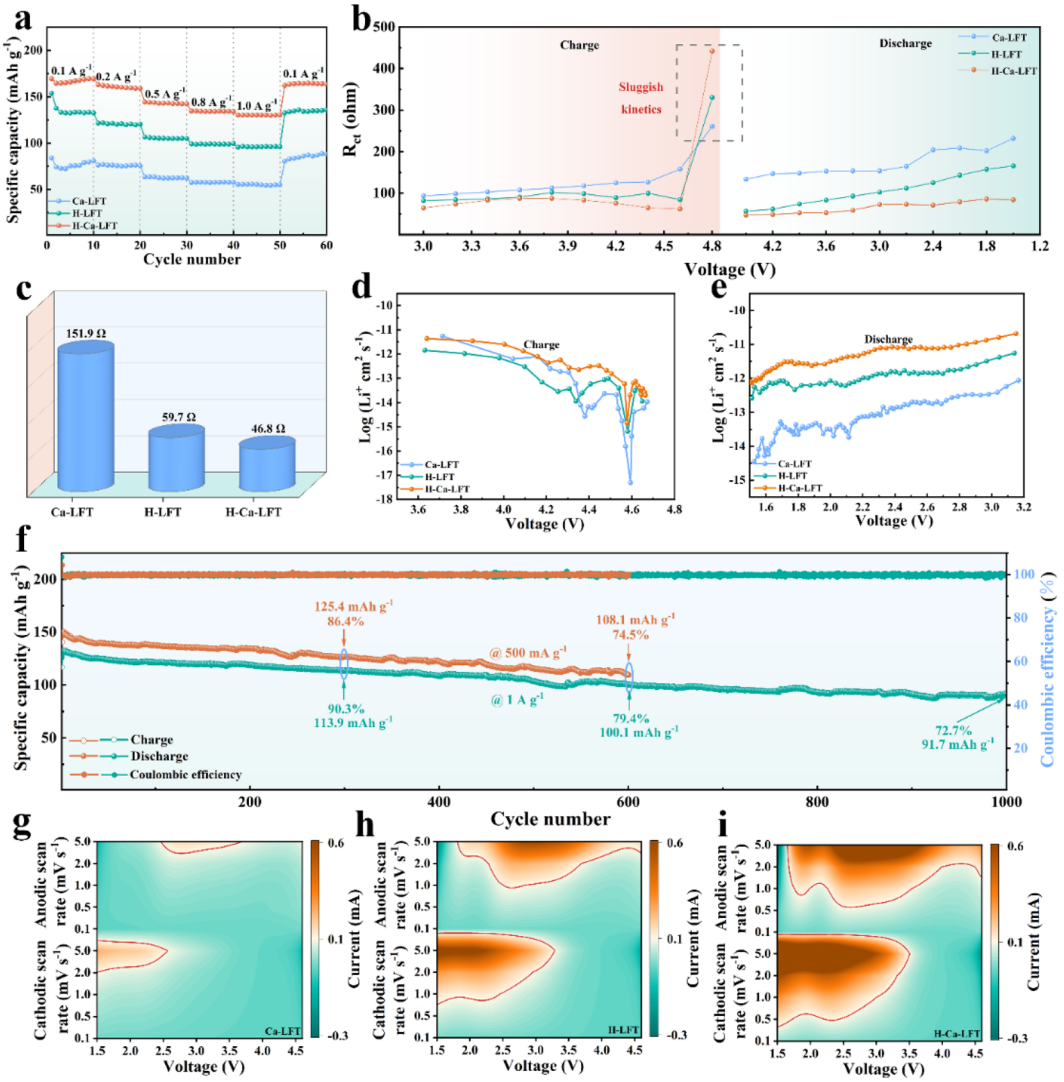

Fig. 4 (a) Rate performances, (b) charge transfer resistance R_{ct} during the first cycle, (c) interfacial layer resistance R_f, (d and e) Li^+ diffusion coefficients of Ca-LFT, H-LFT, and H-Ca-LFT, (f) cycling performances at 500 mA g^{-1} and 1.0 A g^{-1} of H-Ca-LFT, (g–i) contour plots of the CV pattern with different scan rates of Ca-LFT, H-LFT, and H-Ca-LFT.

did not change significantly before and after cycling, which is attributed to the porous structure that can effectively alleviate the volume expansion problem during cycling, thereby demonstrating excellent structural stability. Despite a relatively high current density of 1.0 A g^{-1}, the capacity retention of H-Ca-LFT can be maintained at 72.7% (91.7 mA h g^{-1}), highlighting the impressive long-term cycle stability (Fig. 4f).

Cyclic voltammetry (CV) was conducted to investigate the kinetics of Li^+ transport at scanning rates ranging from 0.1 to 5.0 mV s^{-1} between 1.5 and 4.6 V (Fig. S9a–c†). Fig. 4g–i exhibit the contour plots of the CV patterns for Ca-LFT, H-LFT, and H-Ca-LFT, respectively. The two anodic peaks at 1.85 and 2.60 V correspond to the oxidation of Ti^{3+} to Ti^{4+} and Fe^{2+} to Fe^{3+}. Meanwhile, the two cathodic peaks at 1.50 and 2.32 V result from the reduction of Ti^{4+} and Fe^{3+}. Obviously, H-Ca-LFT shows a higher current response compared to Ca-LFT and H-LFT, especially in the redox regions of Ti^{3+}/Ti^{4+} and Fe^{2+}/Fe^{3+}. Based on the fitted b-values of the log(i) *versus* log(v) plots, it can be concluded that the Li storage in the battery is diffusion controlled or surface controlled. As shown in Fig. S9e and f,† the b values of peak 1/peak 2 for H-LFT and H-Ca-LFT are 0.89/0.81 and 0.92/0.79, respectively, indicating that the Li storage process is mainly controlled by the pseudocapacitive behavior, which facilitates excellent rate charge diffusion.[45] Meanwhile, the b values of peak 1/peak 2 in Ca-LFT are 0.63 and 0.68, suggesting that the electrochemical process is mainly controlled by the diffusion contribution (Fig. S9d†). The pseudocapacitive proportions of Ca-LFT, H-LFT, and H-Ca-LFT are calculated to be 66.9%, 78.7%, and 84.0% at 2.0 mV s^{-1}, respectively (Fig. S9g–i†). Besides, these pseudocapacitive contributions progressively increase with rising scan rates, reaching a considerable pseudocapacitance proportion of 92.5% for H-Ca-LFT at 5.0 mV s^{-1} (Fig. S9l†). Such a high pseudocapacitive contribution is attributed to the Li deficiency

and the rich porous structure of H-Ca-LFT, which displays ultrahigh reactivity and fast Li^+ diffusion kinetics.

The existence of Li deficiency greatly promotes cationic redox and alleviates the high activity of anion oxidation, as revealed by the X-ray photoemission spectroscopy (XPS) analysis. When charged to 4.8 V, all electrodes display a similar trend, with characteristic peaks of Fe^{4+} appearing at about 716.7 eV (Fig. S10a, b† and 5a).[46] As shown in Table S5,† the ratio of Fe^{4+} in Ca-LFT, H-LFT, and H-Ca-LFT is 13.34%, 18.10%, and 21.37%, respectively, suggesting a higher degree of Fe (Fe^{2+} → Fe^{3+} → Fe^{4+}) participation in the oxidation reaction in H-LFT and H-Ca-LFT. Besides, the peaks located at 530.5 eV in the O 1s spectra can be assigned to the peroxo-like O^{n-} (Fig. S10c, d† and 5b). The ratio of O^{n-} in Ca-LFT (47.19%) is much higher than that of H-LFT (16.15%) and H-Ca-LFT (15.20%), showing a more severe anion oxidation reaction in Ca-LFT (Table S6†).[47] However, Ti 2p spectra have no obvious change compared with the original state, indicating that Ti^{4+} is still maintained (Fig. S10e, f† and 5c). Therefore, the capacity predominantly arises from Fe and O during the first charging process. Up discharging to 1.5 V, the Fe 2p spectra of all electrodes shift to lower binding energy, implying a reversible redox reaction (Fig. S10a, b† and 5a). Differently, H-LFT and H-Ca-LFT demonstrate superior reversibility to Ca-LFT, meaning that the Li-deficient structure alleviates irreversible oxygen loss (Fig. S10c, d† and 5b). Besides, the two additional peaks at 457.9 and 463.7 eV are assigned to Ti^{3+} $2p_{3/2}$ and Ti^{3+} $2p_{1/2}$, respectively, demonstrating the reduction of Ti^{4+} to Ti^{3+} (Fig. S10e, f† and 5c).[48] Additionally, Ar^+ sputtering XPS depth profiling is employed to systematically investigate the reaction mechanisms at different depths, revealing consistency between surface redox reactions and bulk redox processes (Fig. S11†). The above results show that the Li deficiency greatly promotes the redox of cations while inhibiting the high activity of anions.

The Li-deficient engineering strategy effectively achieves cation–anion redox regulation and improves the transport kinetics, which is further verified by the first-principles calculations based on the density functional theory method (DFT). The detailed structure is shown in Fig. S12† and 5d, whereas the calculated density of states (DOS) for Li_2FeTiO_4 (LFT) and Li_2-$FeTiO_4$ with Li deficiency (V-LFT) is compared in Fig. 5e and f. At the pristine state, the valence bands of LFT and V-LFT are mainly influenced by the O 2p and Fe 3d orbitals, suggesting the high activity of O and Fe during the de-lithiation process.[49] The conduction band is mainly affected by the Ti 3d orbital, meaning that the Ti^{4+} in the two structures does not participate

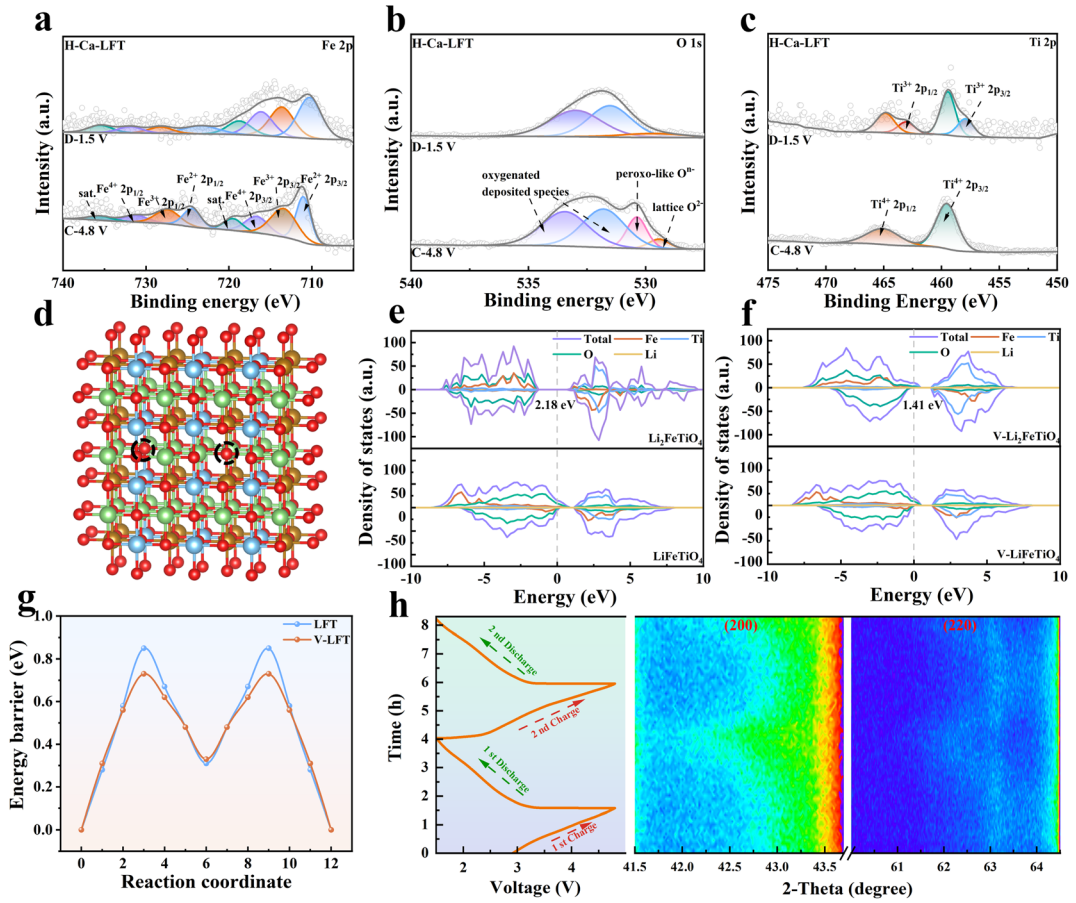

Fig. 5 XPS spectra of (a) Fe 2p, (b) O 1s, and (c) Ti 2p for the H-Ca-LFT electrode at the fully charged and discharged states, (d) crystal structure of V-LFT, (e and f) calculated spin-polarized DOS, (g) Li^+ diffusion energy barrier for LFT and V-LFT, and (h) voltage profiles and contour plots of *in situ* XRD for H-Ca-LFT.

in the oxidation process. Besides, compared with LFT, the band gap between the valence bands and conduction bands in V-LFT is narrower, showing that Li deficiency significantly improves electronic conductivity and promotes rapid charge transfer.[27] A careful analysis reveals that the density of O 2p orbitals in LFT near the Fermi level is higher than that in V-LFT, indicating that the Li-deficient structure suppresses the high redox activity of lattice oxygen, thereby enhancing the reversible anion redox.[50] In a semi-de-lithium structure, the density of O 2p orbitals in LFT and V-LFT near the Fermi level increases, promoting the redox activity of oxygen. The O 2p orbital in LFT quickly moves above the Fermi level, indicating that more lattice oxygen participates in the redox reaction, while this process is alleviated in V-LFT. The calculation results show that the redox of oxygen contributes significantly to the charge compensation process in LFT and V-LFT. However, the introduction of the Li deficiency configuration effectively suppresses the high activity of oxygen through the strong Fe–O interaction.[26] Besides, the nudged elastic band (NEB) method is employed to investigate the diffusion of Li^+ along the migration pathways (octahedron–tetrahedron–octahedron) in LFT and V-LFT. As illustrated in Fig. 5g, the calculated energy barrier for Li^+ diffusion in V-LFT decreases by 120 meV compared to LFT, indicating that the Li-deficient structure accelerates the diffusion of Li^+, thus enhancing the electrochemical kinetic performance.[39]

Furthermore, *in situ* XRD is employed to analyze the influence of the acid etching on the crystal structure evolution. The voltage profiles and corresponding intuitive contour plots of Ca-LFT and H-Ca-LFT during the first two cycles from open-circuit voltage to 4.8 V are displayed in Fig. S13† and 5h. The two characteristic peaks of Ca-LFT and H-Ca-LFT electrodes shift to a higher diffraction angle upon the first charging, indicating the lattice parameter decreases with the extraction of Li. During the first discharging, the (200) and (220) peak positions of Ca-LFT shift to the original state. The difference is that the two characteristic peaks of H-Ca-LFT shift to lower diffraction angles than the original state, which is associated with the insertion of more Li into the structure.[26] Both materials exhibit symmetrical characteristic peak movements in the subsequent second cycle, confirming the reversible structural evolution. Notably, no new peaks emerged during cycling for either material, demonstrating the overall solid solution behavior of Ca-LFT and H-Ca-LFT without any phase transition.[51] Therefore, although the acid etching introduces Li deficiency, it does not affect the reversibility of the structural evolution of H-Ca-LFT during the cycle.

Conclusions

In summary, H-Ca-LFT is proposed as a high-performance cathode for LIBs, showing superior rate capability and cycle stability. This performance is achieved through a design that incorporates an initial Li-deficient and a 3D hierarchical porous architecture. Through the combination of electrochemical tests, *in situ*/*ex situ* characterization analysis, and DFT calculations, the remarkable electrochemical performance of H-Ca-LFT originates from Li deficiency, which facilitates highly efficient ion diffusion, enhances electronic conductivity, and suppresses the high activity of oxygen, thus improving ionic transport kinetics and cycle stability. In addition, the 3D hierarchical porous structure not only provides channels for ion diffusion but also increases active sites for electrochemical reactions. Consequently, benefiting from the synergistic effect between the Li deficiency and 3D hierarchical porous structure, the H-Ca-LFT electrode exhibits a high initial specific capacity of 209.3 mA h g^{-1} at 50 mA g^{-1} and outstanding cycling stability with a capacity retention of 72.7% (91.7 mA h g^{-1}) at 1 A g^{-1} after 1000 cycles. Moreover, it shows excellent rate performance, maintaining 130.4 mA h g^{-1} even at a high current density of 1 A g^{-1}. These findings open up a new direction for the design of cathode materials that possess high rate capability and superior structural stability, which can potentially overcome the challenges of sluggish kinetics and elevated oxygen redox activity for advanced DRX materials.

Data availability

The data supporting this article have been included as part of the ESI.†

Author contributions

Wenjie Ma: data curation, investigation, and writing – original draft. Yakun Tang: conceptualization, supervision, and writing – review and editing. Yue Zhang: data curation and formal analysis. Xiaohui Li: validation and resources. Lang Liu: supervision, funding acquisition and writing – review and editing. Xueting Wang: data curation. Yuliang Cao: conceptualization and formal analysis.

Conflicts of interest

There are no conflicts to declare.

Acknowledgements

This work was supported by the National Natural Science Foundation of China (22278347), the "Tianshan Talents" Science and Technology Innovation Team of Xinjiang Uygur Autonomous Region (2024TSYCTD0002), the Excellent Doctoral Student Research Innovation Project of Xinjiang University of China (XJU2022BS048), and the Postgraduate Innovation Project of Xinjiang Uygur Autonomous Region of China (XJ2023G027).

Notes and references

1 Y. N. Li, Y. Li, H. X. Li, Y. Gan, W. J. Qiu and J. J. Liu, *Nano Energy*, 2024, **119**, 109064.
2 Y. Mahara, H. Oka, T. Nonaka, S. Kosaka, N. T. Takahashi, Y. Kondo and Y. Makimura, *Adv. Energy Mater.*, 2023, **13**, 2301843.

3 J. Qian, Y. Ha, K. P. Koirala, D. Huang, Z. Huang, V. S. Battaglia, C. M. Wang, W. L. Yang and W. Tong, *Adv. Funct. Mater.*, 2023, **33**, 2205972.
4 T. Y. Huang, Z. J. Cai, M. J. Crafton, L. A. Kaufman, Z. M. Konz, H. K. Bergstrom, E. A. Kedzie, H. M. Hao, G. Ceder and B. D. McCloskey, *Adv. Energy Mater.*, 2023, **13**, 2300241.
5 Y. J. Sun, S. C. Jiao, J. Y. Wang, Y. P. Zhang, J. Liu, X. L. Wang, L. Kang, X. Q. Yu, H. Li, L. Q. Chen and X. J. Huang, *J. Am. Chem. Soc.*, 2023, **145**, 11717–11726.
6 S. Guin, S. Ghosh, S. S. Sarkar and U. Maitra, *Chem. Mater.*, 2024, **36**, 10421–10450.
7 S. C. Jiao, Y. J. Sun, J. Y. Wang, D. K. Shi, Y. P. Li, X. K. Jiang, F. W. Wang, Y. P. Zhang, J. Liu, X. L. Wang, X. Q. Yu, H. Li, L. Q. Chen and X. J. Huang, *Adv. Energy Mater.*, 2023, **13**, 2301636.
8 A. Kingan, C. Huang, Z. R. Mansley, R. C. Hill, Z. L. Wang, D. C. Bock, L. Wang, L. Ma, S. N. Ehrlich, J. M. Bai, H. Zhong, C. Jaye, C. Weiland, A. C. Marschilok, E. S. Takeuchi, Y. M. Zhu, S. Yan and K. J. Takeuchi, *ACS Nano*, 2024, **51**, 34776–34790.
9 Z. Y. Lun, B. Ouyang, D. H. Kwon, Y. Ha, E. E. Foley, T. Y. Huang, Z. J. Cai, H. Kim, M. Balasubramanian, Y. Z. Sun, J. P. Huang, Y. Tian, H. Kim, B. D. McCloskey, W. Yang, R. J. Clément, H. W. Ji and G. Ceder, *Nat. Mater.*, 2020, **20**, 214–221.
10 H. Lee, M. Kim, H. Park, Y. Yoo, S. Na, H. D. Lim, J. Kim and W. S. Yoon, *Adv. Funct. Mater.*, 2023, **34**, 2312401.
11 J. Kim, Y. Shin and B. Kang, *Adv. Sci.*, 2023, **10**, 2300615.
12 W. J. Ma, Y. K. Tang, Y. Zhang, X. H. Li, L. Liu, X. T. Wang and Y. L. Cao, *J. Energy Chem.*, 2025, **101**, 42–51.
13 B. Li, M. T. Sougrati, G. Rousse, A. V. Morozov, R. Dedryvère, A. Iadecola, A. Senyshyn, L. Zhang, A. M. Abakumov, M. L. Doublet and J. M. Tarascon, *Nat. Chem.*, 2021, **13**, 1070–1080.
14 S. Zhang, Z. Yang, Y. Lu, W. W. Xie, Z. H. Yan and J. Chen, *Adv. Energy Mater.*, 2024, **14**, 2402068.
15 J. X. Zheng, G. F. Teng, J. L. Yang, M. Xu, Q. S. Yao, Z. Q. Zhuo, W. L. Yang, Q. H. Liu and F. Pan, *J. Phys. Chem. Lett.*, 2018, **9**, 6262–6268.
16 N. Sunariwal, F. Dogan, I. Roy, K. Kumar, D. Nordlund, Q. Ma and J. Cabana, *Adv. Funct. Mater.*, 2023, **34**, 2312010.
17 W. J. Tang, G. J. Zhou, C. Z. Hu, A. F. Li, Z. X. Chen, Z. H. Yang, J. H. Su and W. X. Zhang, *ACS Appl. Mater. Interfaces*, 2023, **15**, 17938–17946.
18 Z. L. Yu, H. Huang, Y. J. Liu, X. Y. Qu, Y. Zhou, A. C. Dou, M. R. Su, H. H. Wu, L. Zhang, K. H. Dai, Z. P. Guo, T. Wan, M. Y. Li and D. W. Chu, *Nano Energy*, 2022, **96**, 107071.
19 M. A. Cambaz, B. P. Vinayan, H. Geßwein, A. Schiele, A. Sarapulova, T. Diemant, A. Mazilkin, T. Brezesinski, R. J. Behm, H. Ehrenberg and M. Fichtner, *Chem. Mater.*, 2019, **31**, 4330–4340.
20 Y. M. Zhang, E. C. Self, B. P. Thapaliya, R. Giovine, H. M. Meyer, L. Z. Li, Y. Yue, D. C. Chen, W. Tong, G. Y. Chen, C. M. Wang, R. Clément, S. Dai and J. Nanda, *ACS Appl. Mater. Interfaces*, 2021, **13**, 38221–38228.
21 F. Wu, J. Y. Dong, J. Y. Zhao, Q. Shi, Y. Lu, N. Li, D. Y. Cao, W. B. Li, J. N. Hao, Y. Zheng, L. Chen and Y. F. Su, *J. Energy Chem.*, 2023, **82**, 158–169.
22 X. Y. Cai, Z. Shadike, N. Wang, L. Liu, E. Y. Hu and J. L. Zhang, *Next Mater.*, 2024, **2**, 100086.
23 B. Zhou, S. Y. An, D. Kitsche, S. L. Dreyer, K. Wang, X. H. Huang, J. Thanner, M. Bianchini, T. Brezesinski, B. Breitung, H. Hahn and Q. S. Wang, *Small Struct.*, 2024, **5**, 2400005.
24 Y. Lee, C. Park and K. Park, *Chem. Mater.*, 2023, **36**, 232–246.
25 J. Ahn, Y. Ha, R. Satish, R. Giovine, L. Z. Li, J. Liu, C. M. Wang, R. J. Clement, R. Kostecki, W. L. Yang and G. Y. Chen, *Adv. Energy Mater.*, 2022, **12**, 2200426.
26 Y. S. Jiang, F. D. Yu, W. Ke, L. Deng, Y. Xia, X. Y. Li, L. F. Que, N. Zhang, L. Zhao and Z. B. Wang, *Adv. Funct. Mater.*, 2023, **33**, 2213615.
27 X. G. Gao, H. Y. Zhang, S. H. Li, S. Zhang, C. H. Guan, X. P. Hu, J. L. Guo, Y. Q. Lai and Z. A. Zhang, *Adv. Funct. Mater.*, 2023, **33**, 2304065.
28 W. J. Ma, Y. K. Tang, Y. Zhang, L. Liu, B. Tang, D. Z. Jia and Y. L. Cao, *Chin. Chem. Lett.*, 2025, **36**, 110346.
29 G. F. Xu, J. L. Li, Q. R. Xue, X. P. Ren, G. Yan, X. D. Wang and F. Y. Kang, *J. Power Sources*, 2014, **248**, 894–899.
30 W. B. Guo, C. Y. Zhang, Y. G. Zhang, L. Lin, W. He, Q. S. Xie, B. S. Sa, L. S. Wang and D. L. Peng, *Adv. Mater.*, 2021, **33**, 2103173.
31 F. Wu, J. Y. Dong, L. Chen, G. Chen, Q. Shi, Y. L. Nie, Y. Lu, L. Y. Bao, N. Li, T. L. Song, S. Chen and Y. F. Su, *Energy Mater. Adv.*, 2023, **4**, 0007.
32 S. Ramakrishnan, B. Park, J. Wu, W. Yang and B. D. McCloskey, *J. Am. Chem. Soc.*, 2020, **142**, 8522–8531.
33 R. J. Wang, Y. X. Zhang, Z. Li, L. Wu, J. R. Chen, X. L. Liu, H. Hu, H. Ding, S. Cao, Q. L. Wei and X. Y. Wang, *J. Energy Chem.*, 2025, **101**, 630–640.
34 V. Soundharrajan, S. Kim, S. Nithiananth, M. H. Alfaruqi, J. J. Piao, D. T. Pham, V. Mathew, S. A. Han, J. H. Kim and J. Kim, *Carbon Energy*, 2024, **6**, e551.
35 J. Wu, X. F. Zhang, S. Y. Zheng, H. D. Liu, J. P. Wu, R. Q. Fu, Y. X. Li, Y. X. Xiang, R. Liu, W. H. Zuo, Z. H. Cui, Q. H. Wu, S. Q. Wu, Z. H. Chen, P. Liu, W. L. Yang and Y. Yang, *ACS Appl. Mater. Interfaces*, 2020, **12**, 7277–7284.
36 Y. J. Zhao, S. X. Zhang, Y. Y. Zhang, J. R. Liang, L. T. Ren, H. J. Fan, W. Liu and X. M. Sun, *Energy Environ. Sci.*, 2024, **17**, 1279–1290.
37 Y. J. Wang, Z. Y. Gu, D. S. Bai, Z. L. Hao, H. W. Huang, Y. Yan, C. J. Li, A. M. Liu and X. L. Wu, *Angew. Chem., Int. Ed.*, 2025, e202507573.
38 K. Zhou, Y. N. Li, Y. Ha, M. J. Zhang, W. Dachraoui, H. D. Liu, C. Y. Zhang, X. S. Liu, F. C. Liu, C. Battaglia, W. L. Yang, J. J. Liu and Y. Yang, *Chem. Mater.*, 2022, **34**, 9711–9721.
39 P. F. Liu, H. Zhang, W. He, T. F. Xiong, Y. Cheng, Q. S. Xie, Y. T. Ma, H. F. Zheng, L. S. Wang, Z. Z. Zhu, Y. Peng, L. Q. Mai and D. L. Peng, *J. Am. Chem. Soc.*, 2019, **141**, 10876–10882.
40 M. Yang, J. Y. Jin, Y. L. Shen, S. J. Sun, X. Y. Zhao and X. D. Shen, *ACS Appl. Mater. Interfaces*, 2019, **11**, 44144–44152.

41 D. Luo, H. Zhu, Y. Xia, Z. J. Yin, Y. Qin, T. Y. Li, Q. H. Zhang, L. Gu, Y. Peng, J. W. Zhang, K. M. Wiaderek, Y. L. Huang, T. T. Yang, Y. Tang, S. Lan, Y. Ren, W. Q. Lu, C. M. Wolverton and Q. Liu, *Nat. Energy*, 2023, **8**, 1078–1087.
42 J. S. Yang, P. Li, F. P. Zhong, X. M. Feng, W. H. Chen, X. P. Ai, H. X. Yang, D. G. Xia and Y. L. Cao, *Adv. Energy Mater.*, 2020, **10**, 1904264.
43 S. Y. Zhou, Y. X. Sun, T. Gao, J. H. Liao, S. X. Zhao and G. Z. Cao, *Angew. Chem., Int. Ed.*, 2023, **62**, e202311930.
44 X. Y. Cai, Z. Shadike, N. Wang, X. L. Li, Y. Wang, Q. F. Zheng, Y. X. Zhang, W. X. Lin, L. S. Li, L. W. Chen, S. Y. Shen, E. Y. Hu, Y. N. Zhou and J. L. Zhang, *J. Am. Chem. Soc.*, 2025, **147**, 5860–5870.
45 X. J. Zhang, J. Xie, Z. J. Lu, Y. K. Tang, Y. Wang, J. D. Hu and Y. L. Cao, *J. Colloid Interface Sci.*, 2024, **667**, 385–392.
46 R. Fong, N. Mubarak, S. W. Park, G. Lazaris, Y. W. Liu, R. Malik, D. H. Seo and J. Lee, *Adv. Energy Mater.*, 2024, **14**, 2400402.
47 Q. W. Cui, Y. Li, Y. N. Li, W. J. Qiu and J. J. Liu, *ACS Nano*, 2024, **18**, 2302–2311.
48 C. X. Zhu, Y. K. Tang, L. Lang, R. Sheng, X. H. Li, Y. Cao and Y. N. NuLi, *J. Colloid Interface Sci.*, 2021, **581**, 307–313.
49 Y. Kobayashi, M. Sawamura, S. Kondo, M. Harada, Y. Noda, M. Nakayama, S. Kobayakawa, W. Zhao, A. Nakao, A. Yasui, H. B. Rajendra, K. Yamanaka, T. Ohta and N. Yabuuchi, *Mater. Today*, 2020, **37**, 43–55.
50 K. Wu, P. L. Ran, W. Yin, L. H. He, B. T. Wang, F. W. Wang, E. Y. Zhao and J. K. Zhao, *Angew. Chem., Int. Ed.*, 2024, e202410326.
51 T. Jin, P. F. Wang, Q. C. Wang, K. J. Zhu, T. Deng, J. X. Zhang, W. Zhang, X. Q. Yang, L. F. Jiao and C. S. Wang, *Angew. Chem., Int. Ed.*, 2020, **59**, 14511–14516.